J. Space Weather Space Clim. 2018, 8, A05

https://doi.org/10.1051/swsc/2017047

SWSC

Available online at:
www.swsc-journal.org

Space weather effects on GNSS and their mitigation

RESEARCH ARTICLE

OPEN ACCESS

Feasibility of precise navigation in high and low latitude regions under scintillation conditions

José Miguel Juan[1,*], Jaume Sanz[1], Guillermo González-Casado[1], Adrià Rovira-Garcia[1], Adriano Camps[1,2], Jaume Riba[1], José Barbosa[3], Estefania Blanch[4], David Altadill[4] and Raul Orus[5]

[1] Universitat Politècnica de Catalunya & IEEC/CTE-UPC, UPC Campus Nord, 08034 Barcelona, Spain
[2] Institut d'Estudis Espacials de Catalunya IEEC/UPC, Edifici Nexus-201, 08034 Barcelona, Spain
[3] RDA - Research and Development in Aerospace GmbH, Rigiplatz 5, 8006 Zürich, Switzerland
[4] Observatori de l'Ebre, CSIC – Universitat Ramon Llull, 43520 Roquetes, Spain
[5] European Space Agency (ESA ESTEC), Keplerlaan 1, 2201AZ Noordwijk, Netherlands

Received 21 June 2017 / Accepted 15 December 2017

Abstract – Scintillation is one of the most challenging problems in Global Navigation Satellite Systems (GNSS) navigation. This phenomenon appears when the radio signal passes through ionospheric irregularities. These irregularities represent rapid changes on the refraction index and, depending on their size, they can produce also diffractive effects affecting the signal amplitude and, eventually producing cycle slips. In this work, we show that the scintillation effects on the GNSS signal are quite different in low and high latitudes.

For low latitude receivers, the main effects, from the point of view of precise navigation, are the increase of the carrier phase noise (measured by σ_ϕ) and the fade on the signal intensity (measured by S4) that can produce cycle slips in the GNSS signal. With several examples, we show that the detection of these cycle slips is the most challenging problem for precise navigation, in such a way that, if these cycle slips are detected, precise navigation can be achieved in these regions under scintillation conditions.

For high-latitude receivers the situation differs. In this region the size of the irregularities is typically larger than the Fresnel length, so the main effects are related with the fast change on the refractive index associated to the fast movement of the irregularities (which can reach velocities up to several km/s). Consequently, the main effect on the GNSS signals is a fast fluctuation of the carrier phase (large σ_ϕ), but with a moderate fade in the amplitude (moderate S4). Therefore, as shown through several examples, fluctuations at high-latitude usually do not produce cycle slips, being the effect quite limited on the ionosphere-free combination and, in general, precise navigation can be achieved also during strong scintillation conditions.

Keywords: ionosphere (aurora) / ionosphere (equatorial) / positioning system / irregularities / algorithm

1 Introduction

Ionospheric scintillation is one of the most challenging effects affecting precise positioning in Global Navigation Satellite Systems (GNSS). This perturbation is related with fluctuations in the intensity and the phase of electromagnetic signals when they are refracted and/or diffracted by irregularities in the electron distribution encountered during their travel along the ray propagation path. In this way, scintillation produces in the GNSS signals an increase of the noise level that can end in a loss of lock on the receiver tracking, thereby disrupting the performance of space-based communication and navigation systems. Therefore, the identification, correction or mitigation of the scintillation effects is one of the current challenges in achieving precise GNSS navigation (Pi et al., 2017).

There are two common parameters to characterize the intensity (or amplitude) and the phase scintillation. Amplitude scintillation is characterized through the S4 parameter (Briggs & Parkin, 1963) which is defined as the normalized standard deviation of the signal intensity: due to diffractive effects, the amplitude of the signals suffers deep fades (decreasing dramatically their C/N_0) which can end in a cycle slip of the carrier phase tracking or even a loss of lock. Whereas, phase scintillation is measured trough the σ_ϕ parameter (Yeh & Chao-Han, 1982), which is the standard deviation of the high frequency fluctuation of the carrier phase. These fast fluctuations can be due to the diffractive effect on the carrier

*Corresponding author: jose.miguel.juan@upc.edu

phase, but also to the fast movement of ionospheric irregularities, which are typical of the auroral (or polar) regions and can achieve velocities larger than 1 km/s (Forte & Radicella, 2002). In order to measure such standard deviation a previous detrending is needed which is done usually by applying a Butterworth filtering to the signal, but this filtering requires special receivers, Ionospheric Scintillation Monitoring Receivers (ISMRs), which are high level receivers that usually work with a sampling rate of 50 Hz. In order to avoid receiver clock instabilities that could be interpreted as ionospheric scintillation (Humphreys et al., 2005), ISMRs are equipped with a very stable oscillator. But, more recently, in Juan et al. (2017), it has been proposed a new method that allows the detrending using conventional GNSS receivers without requiring a very stable receiver clock (i.e. an atomic clock). This new method, named geodetic detrending, has opened the possibility to do long term studies about scintillation using the high-rate International GNSS Service (IGS) network which is a network of geodetic receivers working at 1 Hz and worldwide distributed.

Several studies have been carried out about the climatology of ionospheric scintillation (e.g. Cervera & Thomas, 2006; Paznukhov et al., 2012), from these studies, it is possible to state that the occurrence of ionospheric scintillation and its intensity strongly depend on latitude, local time, season of the year, solar cycle, and magnetic activity, presenting a strong degree of day to day variability (Aarons, 1982, 1993). Regarding the latitude dependency, it is well known (e.g. Béniguel et al., 2009; Sanz et al., 2014) that, basically, the regions affected by scintillation are the high latitude regions (i.e. regions with a geomagnetic latitude, $|\mathrm{GMLAT}| > 60°$) and the low latitude regions ($|\mathrm{GMLAT}| < 30°$). But the origin of scintillation is different in these two regions. Indeed, high latitude scintillation appears to be associated with geomagnetic storms or solar events, whereas in equatorial latitudes, it is associated with plasma movements (bubbles) that typically occur after the local sunset. Moreover, the characteristics of scintillation are also different in those two regions (e.g. Béniguel et al., 2009; Juan et al., 2017): in high-latitude regions, phase scintillation predominates being the amplitude scintillation usually moderate, therefore carrier phase cycle slips are not frequent. In low latitude regions not only phase scintillation but also amplitude scintillation is important and the GNSS signals can experience frequent cycle slips. These different regional characteristics of scintillation have distinct effects on navigation.

In recent years some works have been focused on the impact of scintillation in precise positioning. Using data collected by a high latitude receiver placed at $\mathrm{GMLAT} = 66°$, Pi et al. (2017) showed a clear degradation on the accuracy of the positioning from around 5 cm during quiet ionospheric conditions to close to 1 m when scintillation is present ($\mathrm{DST} < -100$ nT). Jacobsen & Andalsvik (2016) studied also the effect of scintillation on the positioning of four high latitude receivers ($60° < \mathrm{GMLAT} < 67°$) during the St. Patrick's day storm ($\mathrm{DST} < -200$ nT). In their study they found only a slight worsening of the position accuracy when the position is computed under scintillation conditions, but it has to be taken into account that the σ_Φ values of the cases they presented were smaller than 0.4 radians, i.e. it cannot be considered as strong scintillation. More recently, Juan et al. (2017) analysed the GNSS data collected under scintillation conditions by four receivers placed in high and low latitude regions (GMLATs around −78, −12, −11 and 69°), during February 27th in 2014, i.e. a day close to the equinox in the last solar maximum and when a geomagnetic storm occurred ($\mathrm{DST} \sim -100$ nT) affecting the high latitude observations. From this study it is concluded that the main effect on navigation is associated to the occurrence of cycle slips in the GNSS signal, being these cycle slips much more frequent at low latitudes. From this point, they suggested that, under scintillation, precise navigation with two frequency signals could be possible in high latitude regions at the same level of accuracy than during quiet ionospheric conditions. However, in low latitude regions one should expect degradation on the position accuracy due to the non-refractive character of scintillation in such regions.

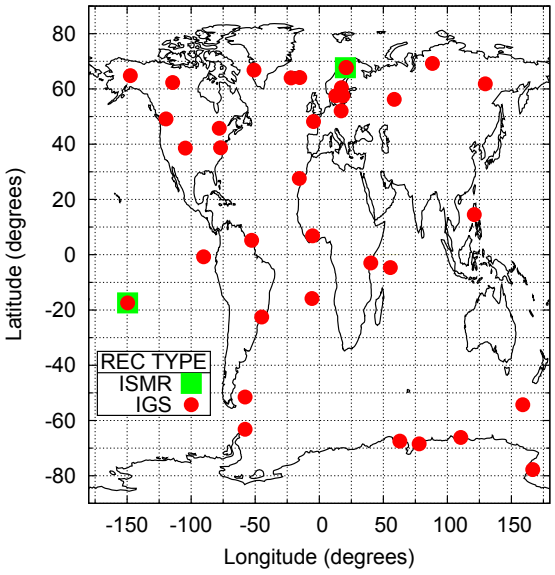

Fig. 1. Map with the receivers used in this work. IGS receivers (red circles). ISMR receivers (green squares).

In the present work we apply the geodetic detrending presented in Juan et al. (2017) in order to show the feasibility of achieving precise positioning under scintillation conditions in high and low latitude regions. In Section 2, we describe the data that we use for obtaining the results of this work. In Section 3 we present the results in two parts, the first part is devoted to show how, thanks to the geodetic detrending, we are able to see the scintillation effects on the signal (in particular the cycle slips) and, in the second part, we present the results on navigation. Finally, in Section 4 we present the conclusions of this work.

2 Data

The results presented in this work were obtained in the framework of the European Space Agency (ESA) project named SCIONAV (ESA-ITT 1-8214/15/NL/LvH). One of the goals of SCIONAV is to characterize the effect of the ionospheric scintillation on the GNSS signal in high and low latitude regions. As part of this project, we have analysed the data gathered under ionospheric activity for a set of 35 permanent receivers which are depicted in Figure 1. These receivers correspond to IGS receivers, i.e. geodetic receivers which are collecting data at 1 Hz, but, two of them, KIR1 in

Table 1. List of receivers whose data are analysed in this work.

RCV name	Network	LON (°)	LAT (°)	GMLT (°)	Receiver type	Sampling rate
KIR0	IGS	21.07	67.74	65.30	JAVAD TRE_G3TH DELTA	1 Hz
KIRU	IGS	20.97	67.72	65.29	SEPT POLARX4	1 Hz
KIR1	MONITOR	20.41	67.71	65.36	SEPT POLARXS	50 Hz
YELL	IGS	−114.48	62.32	68.57	JAVAD TRE_G3TH DELTA	1 Hz
KOUR	IGS	−52.81	5.22	14.24	SEPT POLARX4	1 Hz
MAL2	IGS	40.19	−2.98	−6.64	SEPT POLARX4	1 Hz
FAA1	IGS	−149.61	−17.44	−15.06	SEPT POLARX4	1 Hz
FAAS	MONITOR	−149.61	−17.44	−15.06	SEPT POLARXS	50 Hz

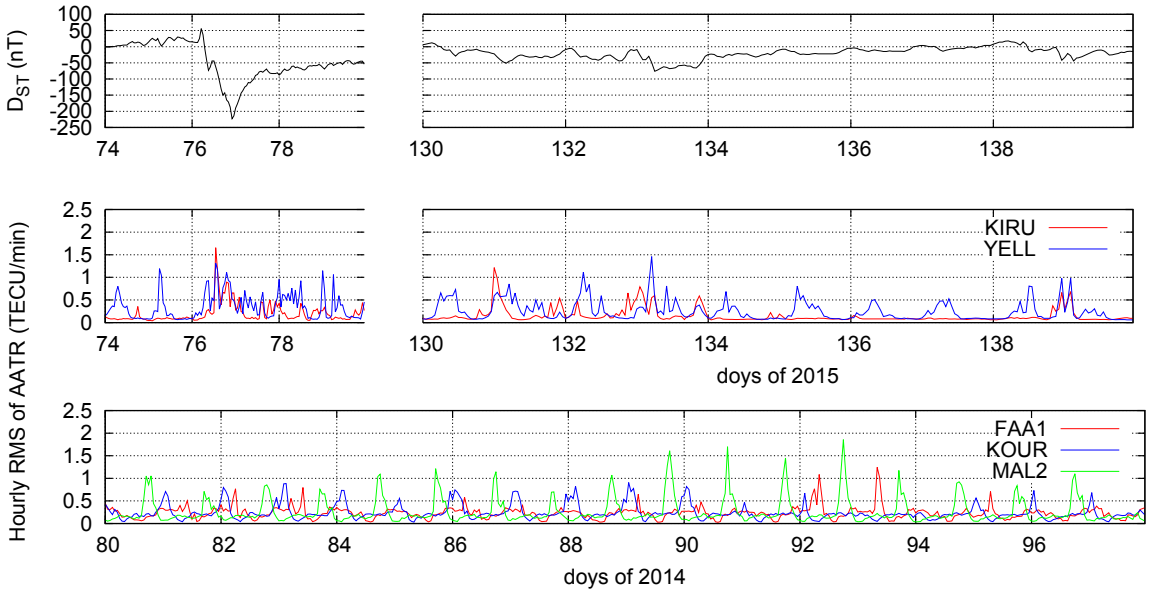

Fig. 2. Magnetic and ionospheric activity during the periods studied in this work. Top panel: DST during the period when the high latitude data is analysed in 2015. Middle panel: AATR for the high latitude receivers (KIRU and YELL). Bottom panel: AATR for the low latitude receivers (KOUR, MAL2 and FAA1) during the analysed period in 2014.

Sweden and FAAS in Tahiti, are ISMRs which belong to the ESA MONITOR project, working at 50 Hz and providing also the typical ionospheric scintillation index S4 and σ_ϕ.

As it is well known in the navigation/positioning topics, frequently it is hard to distinguish whether a positioning error is due to the ionospheric disturbances or to other causes (for instance, bad geometries). This is the reason why we have preferred to use the best environments (i.e. permanent geodetic stations) in order to minimize other errors than those induced by the ionospheric disturbances. In this sense, for the positioning assessment we have preferred to use the data from IGS receivers rather than those from the MONITOR receivers. Indeed, the IGS receivers are well characterized with precise coordinates, well known antenna calibration and also zenith tropospheric delays values can be easily obtained. On the contrary, there is no information about the antenna type of the MONITOR receivers, moreover there are no precise coordinates nor tropospheric delay values. Although these values can be computed with our tools, this could be an additional error source that would degrade the geodetic detrending. However, in order to better characterize the ionospheric disturbances, it is worth to cross check the ionospheric perturbation index, extracted from receivers working at 1 Hz, with those extracted directly from the ISMR collocated receivers, which are computed from the data collected at 50 Hz.

From the previous considerations, in spite of having obtained routinely results for the 35 receivers, the results presented in this work correspond to a reduced set of them, in such a way that they must be collocated with an ISMR (i.e. with FAAS and KIR1), but we also select receivers to have a wide coverage in the regions with ionospheric activity. The coordinates of this set of receivers are shown in Table 1.

In order to select the days for processing the data, we have taken into account the availability of the ISMR data and the ionospheric activity. In this sense, for the low latitude receivers, we have processed the data collected during the days of year (DoY) 80–97 in 2014, i.e. more than 2 weeks around the spring equinox and in the maximum of the last solar cycle. For the high latitude receivers we have selected 2

periods in 2015, the first period ranges from DoY 74 to the DoY 79 which includes the St. Patrick's day storm (see for instance Jacobsen & Andalsvik, 2016) and the second period correspond to the range of DoYs 130–139, in these two periods all the high latitude receivers present ionospheric events with strong scintillation ($\sigma_\phi > 1$).

Figure 2 depicts the ionospheric activity during the set of days studied in this work. The activity is characterized by means of the well-known geomagnetic index DST and the Along Arc TEC Rate index (AATR), defined in Sanz et al. (2014). From the DST index, one can see that the most disturbed period corresponds to the days during the St. Patrick's day storm (see for instance Jacobsen & Andalsvik, 2016), being the second period quieter than the first one. However, during this second period, several ionospheric disturbances, which last for some hours, can be observed from the AATR values. As we will see later, these ionospheric disturbances can also be associated to relevant values of scintillation activity (Andalsvik & Jacobsen, 2014). On the other hand, the ionospheric activity for the low latitude receivers is characterized in the bottom panel by means of the AATR. As it is well known (see for instance Béniguel et al., 2009; Sanz et al., 2014 or Jiao & Morton, 2015) the ionospheric activity at low latitudes appears linked to equatorial plasma bubbles, which start after the sunset hours, regardless the DST (which is defined in a global context). The solar flux during this period of 2014 is maintained around 150 SFU.

As it was shown in Juan et al. (2017), one of the main effects of scintillation is the occurrence of cycle slips (mainly at low latitude). Therefore, in order to obtain the navigation solution, one has to detect such cycle slips and to exclude the data gathered during the cycle slip occurrence. But this data exclusion can reduce the usable data in some epochs and can result in poor satellite geometries. In order to mitigate these weak geometries (see for instance Moraes et al., 2017b), we have used data from the GPS and GLONASS constellations. In this way we have been able to process all the epochs with a large number of satellites. However, in the case of the YELL receiver only GPS data was available, so the results are obtained with only this constellation, however this is not a problem because cycle slips are much less frequent in high latitude.

3 Results

In this section we will show some of the results we have obtained by processing the data described in the previous section. We present the results in two parts, the first one is devoted to explain the results obtained with the technique used for detrending the data (the geodetic detrending) and the second one to show how, applying this technique, it is possible to achieve accurate navigation under scintillation conditions.

3.1 Assessing scintillation applying the geodetic detrending

The geodetic detrending was introduced in Juan et al. (2017) and basically consists on a precise modelling of the different effects on the GNSS signals (except the ionospheric ones). Indeed, thanks to the IGS one can have access to different products (specifically satellite orbits, clocks and receiver zenith tropospheric delays) with an accuracy of few centimetres. Therefore, the receiver measurements can be corrected using these precise corrections without increasing significantly their errors. After these corrections are applied to the GNSS carrier phase measurements, the only remaining residual terms are from the receiver clock, the carrier phase ambiguities and the ionospheric effects. The refractive part of the ionospheric effect can be cancelled out by building the so called ionosphere free combination of carrier phases (L_{IF}). Using the L_{IF} residuals, as it is shown in Juan et al. (2017), it is easy to estimate the receiver clock variation as the common pattern of the L_{IF} residuals for all the satellites in view. Then, once the receiver clock is estimated and subtracted from the measurements (i.e. L_{IF} residuals), only the carrier phase ambiguity is present (a constant per arc). Consequently, any cycle slip in L1 (48 cm in the L_{IF} residual) or L2 (38 cm in the L_{IF} residual) can be easily identified provided that the applied corrections are accurate enough (few centimetres).

In Juan et al. (2017) the geodetic detrending was used for detecting cycle slips and for measuring the non-refractive effects of the ionosphere in the L_{IF} residuals. In this way, it was defined the ionosphere free sigma (σ_{IF}) as the standard deviation of the L_{IF} residuals which accounts for the non refractive effects of scintillation. However, the same technique can be applied to any un-combined carrier phase measurement in order to isolate the ionospheric effect in the measurement. In this way, one can compute the standard phase scintillation parameter σ_ϕ over the ionospheric component of the signal, after applying a High Pass Filtering (HPF), without requiring an ISMR.

Figure 3 shows an example of that for the data gathered by the high-latitude ISMR KIR1 from the GPS satellite PRN30 during the day 133 in 2015. In the top panel it is shown the geodetic detrending of the L_{IF} and L1 (in black and red respectively) which are compared with a 6-order polynomial detrending of the L1 (in blue). On one hand, it can be noticed that the noise of the detrended L_{IF} is at the level of few cm, so almost all the ionospheric effects (including the fast fluctuations) are cancelled out by doing this combination and, on the other hand, the fast fluctuations of the ionospheric delays, in L1, are similar after the two detrendings, that means that the σ_ϕ will be equivalent when applying any of both detrendings. This is not true in general, because, unlike the geodetic detrending, the residual part of the polynomial detrending could include other high frequency effects such as the receiver clock that would be confused as ionospheric effects.

In the bottom panel of Figure 3, it is depicted the σ_ϕ of L1, L5 and L_{IF} (red, green and black, respectively) applying the geodetic detrending over the data from the RINEX file (at 1 Hz). Moreover, in the same panel, it is depicted the L1 σ_ϕ from the output of the ISMR receiver working at 50 Hz (in cyan). In order to facilitate the comparisons, the L5 σ_ϕ is re-scaled to the ionospheric effect on the L1 frequency in length units and all the σ_ϕ are presented in centimetres (3 cm in L1 = 1 radian). This rescaling is done by multiplying the L5 σ_ϕ (in length units) times the ratio of the squared frequencies $((f_1/f_5)^2 = 1.79$ in length units or $f_1/f_5 = 1.34$ if σ_ϕ is in phase units). From the comparison of the σ_ϕ values, one has to note the

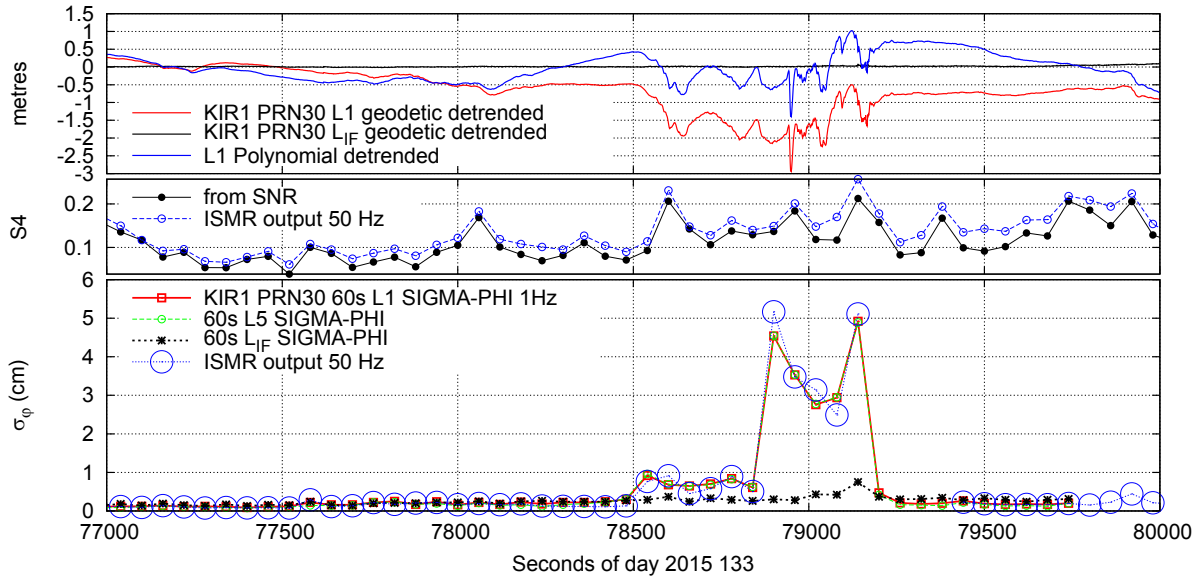

Fig. 3. Example of the geodetic detrending over the measurements of the high latitude receiver KIR1. Top panel: geodetic detrending over the L1 (red) and L_{IF} (black) polynomial detrending over L1 (blue). Middle panel: S4 computed using the SNR measurements (black) and the output from the ISMR (cyan). Bottom panel: σ_ϕ of the different approaches. L1 after the geodetic detrending (red), L5 after the geodetic detrending and rescaled (green), L_{IF} after the geodetic detrending (black) and output from the ISMR (cyan).

equivalence of the σ_ϕ in L1 and L5 computed from the 1 Hz data. This is a consequence of the refractive nature of the scintillation and, because of this, the L_{IF} combination is almost unaffected by scintillation, as can be seen on its σ_ϕ. This agrees with the high correlation found in Jiao & Morton (2015) between the σ_ϕ values at high latitude (a proportionality factor of 1.32). Moreover, there is a good equivalence between the σ_ϕ computed at 50 Hz (output from the ISMR, in blue circles) and the σ_ϕ values computed from 1 Hz data (in black stars). The differences between these σ_ϕ values can be due to the different algorithm used in our computation with respect to the internal computation of the ISMR. Finally, it is worth to notice that these large values of phase scintillation are not linked to large values of S4. This can be seen in the middle panel of Figure 3 where the S4 gathered from the ISMR receiver (in blue circles) is compared with the S4 computed from the SNR measurements in the RINEX file (black dots).

With the previous example, we have illustrated the characterization of scintillation effects using the geodetic detrending for one case of high latitude scintillation. In what follows, we will develop a case for low latitude scintillation. The low latitude case corresponds to the receiver KOUR, in the French Guyenne, and the GPS PRN01. The data was gathered during the DoY 83 in 2014. The top panel in Figure 4 includes the C/No for the L1 and L2 signals where one can see the fades on the amplitude in L2 and also in smaller scale at L1, which are typical in low latitude scintillation. The middle panel depicts the geodetic detrending of the L_{IF} combination which shows that the amplitude fades produce cycle slips in the L2 signals (jumps of 38 cm) that can last up to a few seconds, as it was shown in Juan et al. (2017). These cycle slips are associated to the deep fades of the signal intensity which are much more frequent on the L2 signal, but also affect to the L1 frequency as can be seen by the S4 parameter (computed from the SNR) which is depicted in the middle panel. The bottom panel depicts the standard deviation of the detrended signals L1, L2 and L_{IF}, where the presence of the 2 peaks in L2 and L_{IF} is clearly related with the 2 cycle slips in the L2 frequency. Therefore, such large values of σ_ϕ are, in part, artifacts of the receiver tracker. On the contrary, the signal in L1 only has an increase of its high frequency fluctuations that produce an increase on its σ_ϕ values. This indicates that, unlike the high latitude example, some high frequency effect is still present on the L_{IF} which reflects the fact that part of the scintillation is not refractive, as one can also see in the S4 values.

3.2 Results on navigation

Several authors have pointed out previously (e.g. Pi et al., 2017) that one of the main problems for achieving precise navigation under scintillation conditions is the occurrence of cycle slips. However, in the previous section we have seen that they can be identified from the geodetic detrending of the L_{IF} and even it is possible to distinguish between cycle slips in L1 and L2. In this section we will see how the precise navigation can take benefit of this cycle slip detection by means of the navigation with the data presented in Section 2. For this purpose we have applied the standard precise point positioning (PPP) technique (see for instance Zumberge et al., 1997) in kinematic mode (i.e. the coordinates of the receiver are treated as a white noise process). The navigation filter is restarted every day and runs only in forward mode, so it will last some time (convergence time) before a converged solution can be obtained. We have chosen this processing strategy in order to show the navigation results in a straight forward manner.

Figure 5 depicts three navigation solutions for the high latitude receiver KIRU during the day 133 in 2015. During this day scintillation activity was present during the first and last hours of the day, and this is shown in the top panel of the figure

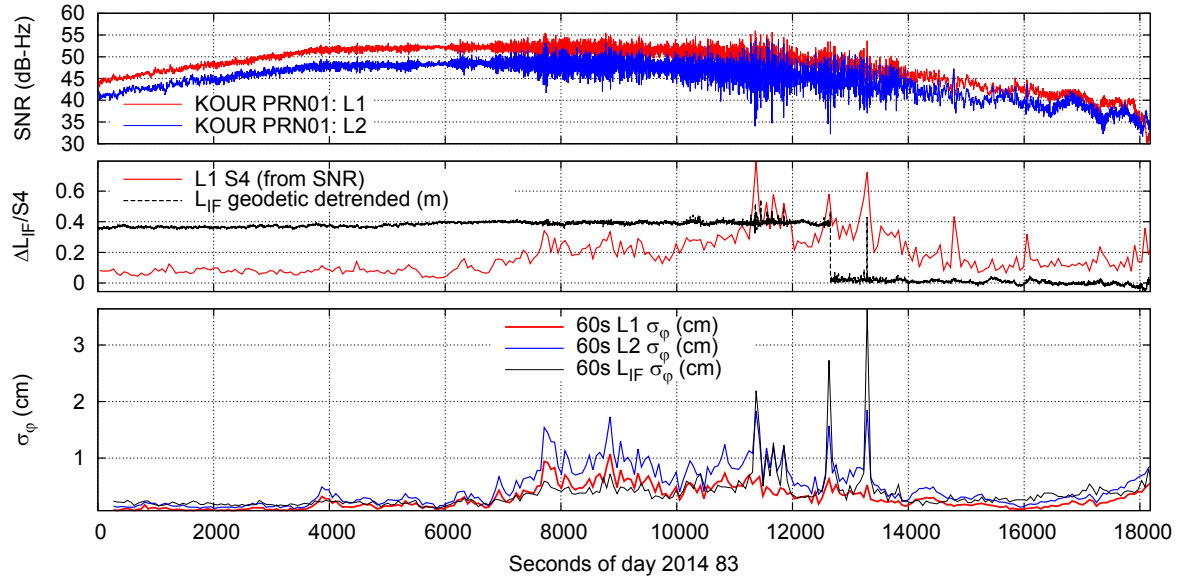

Fig. 4. Example of the geodetic detrending over the measurements from PRN01 collected by the low latitude receiver KOUR, DoY 83, 2014. In the top panel it is depicted the SNR in L1 (red) and in L2 (blue). Middle panel depicts the geodetic detrending of the $L_{IF.}$ The bottom panel depicts the standard deviation of the detrended L1 (red), L2 (blue) and L_{IF} (black).

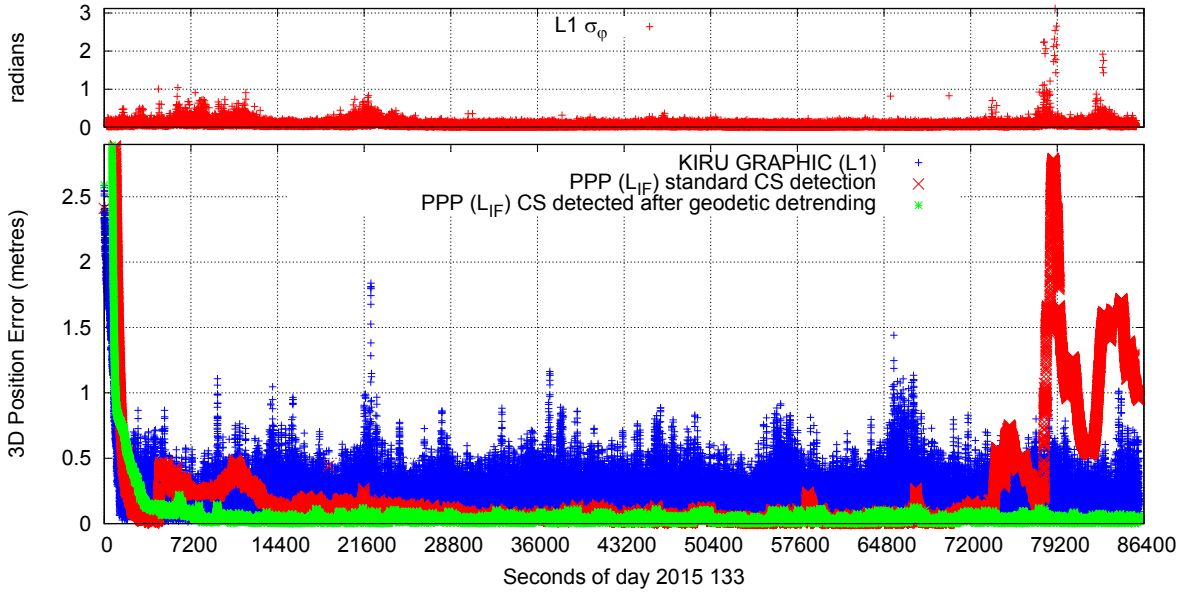

Fig. 5. Example of navigation under scintillation conditions for the high latitude receiver KIRU during the DoY 133, 2015. Top panel: L1 σ_ϕ for all the satellites in view. Bottom panel: navigation using the GRAPHIC combination (blue), navigation using the L_{IF} combination with a standard cycle slip detector (red) and navigation using the L_{IF} combination detecting cycle slips with the geodetic detrending (green).

by means of the σ_ϕ on the L1 signal where it can be seen values of σ_ϕ close or larger than 1 radian.

In the bottom panel (in blue) we depict the navigation solution using the GRoup And PHase Ionospheric Combination (GRAPHIC) that, as it is known (Yunck, 1993), is a ionospheric-free combination between the pseudorange and the carrier phase at the L1 frequency. One can see that the navigation solution is at the submetre level of accuracy, which is the expected accuracy in quiet ionospheric conditions. This accuracy is achieved in spite of the large σ_ϕ values on L1. But these large values are not associated to cycle slips in L1 (but to the code noise involved in the GRAPHIC combination) and the navigation solution has been obtained with at least 14 satellites in all the epochs. Therefore, from this rough navigation solution, it can be concluded that the navigation using the GRAPHIC combination seems to be quite unaffected by scintillation.

Using the L_{IF} combination and applying PPP one should expect navigation errors at the centimetre level. However, this is not the case (red points), indeed, during some periods which are related with high ionospheric activity (see the σ_ϕ depicted

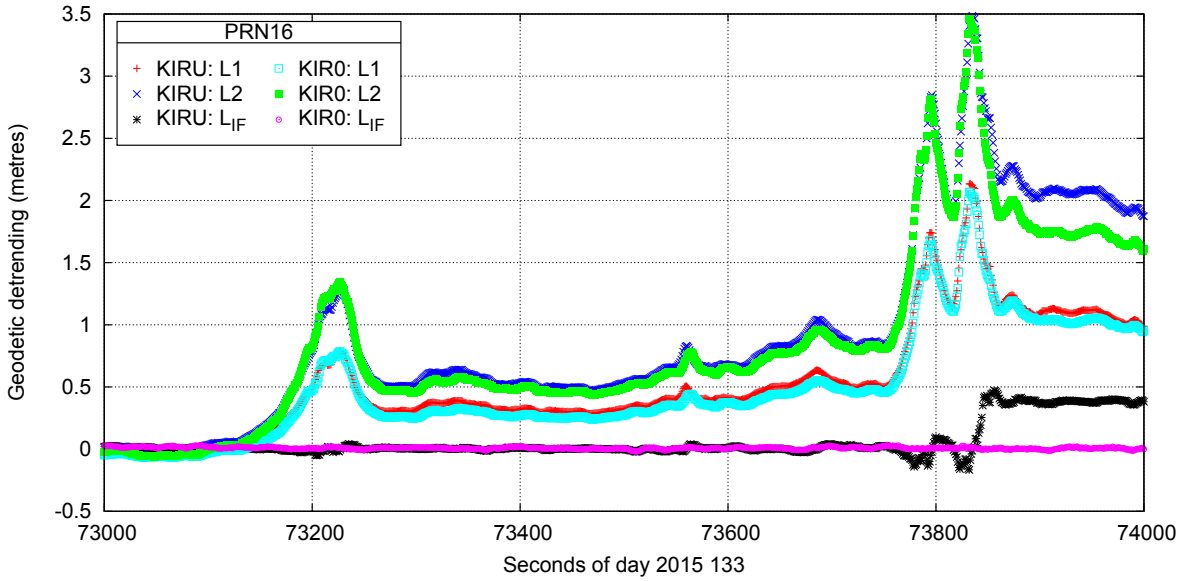

Fig. 6. Geodetic detrending over the signals from PRN16 measured by the high latitude KIRU receiver during the DoY 133, 2015. Ionospheric delay in L1 (red), in L2 (blue) and the residual of the L_{IF} (black). The geodetic detrending over the L1, L2 and L_{IF} signals collected by KIR0 are also depicted in green, cyan and fuchsia respectively.

in the top panel), the navigation error increases in more than 1 order of magnitude with respect to the solution during quiet ionospheric activity, which agrees with the results presented in Pi et al. (2017). These anomalous results are produced by the presence of cycle slips that are not detected using a conventional cycle slip detector, for instance the Turboedit algorithm (Blewitt, 1990).

Indeed, if we apply the geodetic detrending over some of the measurements, one can clearly see these cycle slips. Figure 6 illustrates this. The case corresponds to the satellite PRN16, where the geodetic detrending has been applied to the carrier phases L1 and L2 being the corresponding residuals linked to the ionospheric delays on each signal (red and dark blue crosses), and also over the L_{IF} combination (black points). As can be seen after second 73800 there is a cycle slip in L2 (jump of 38 cm in the detrended L_{IF}), this cycle slip is hard to see by simply looking at the ionospheric delays in L1 or L2, as the Turboedit algorithm does (notice that the carrier phase ambiguity changes but in a continuous manner instead of a discontinuity). Moreover, in the same figure it is depicted the equivalent detrended signals for a close receiver KIR0 (2 km apart), where the ionospheric effect on L1 and L2 are depicted with cyan and green squares, respectively. It can be seen the similar ionospheric disturbances which affect both receivers, but, unlike KIRU, there is not a cycle slip in KIR0 (the detrended L_{IF}, in magenta, does not have a jump), so the presence of cycle slips depends also on the receiver configuration.

Therefore, the conclusion is that these cycle slips are producing this worsening on the navigation solution. This is confirmed if we flag the cycle slips as they are seen from the geodetic detrending. Indeed, after the detection of the cycle slips the errors of the navigation solution are of only some centimetres (green points in Fig. 5), i.e. the expected accuracy using PPP.

The next Figure 7 shows the navigation of the receiver KIRU during a period of 6 days around the St. Patrick's day storm (17th March in 2015, DoY 076).

Figure 7 depicts, in red, the scintillation activity measured by means of the σ_ϕ (bottom panel). From the σ_ϕ values one can see events of strong scintillation as it was already reported by previous works during the St. Patrick's day storm. However, as it can be seen in the top panel in red, the amplitude scintillation, from the maximum S4 values, is very low, as it is expected for high latitude (see, for instance, Jiao & Morton, 2015) and, equivalently the σ_{IF} (see Juan et al., 2017), which is depicted in black, is just of few centimetres under these severe phase scintillation conditions. In the same bottom panel of the figure the number of satellites (divided by 10) used for computing the navigation solution is depicted by a black line. This number is maintained almost all the time above 15, that means that the number of measurements discarded by jumps in the carrier phase are actually quite low, even during the strongest scintillation periods. This result confirms those obtained in Juan et al. (2017) where it was stated that the carrier phase jumps due to scintillation are not very frequent in high latitude scintillation. Finally, the navigation solution is depicted by green points where one can see that, except for the first hours of each day (every day the navigation filter is reseted), the accuracy of the navigation solution is maintained at the level of few centimetres, which is the expected accuracy in quiet ionospheric conditions.

Figure 8 depicts a similar example like in Figure 7 but now for the low latitude receiver FAA1. Here scintillation is associated to the ionospheric depletions that in low latitude appear after the sunset hours. As it can be seen in the top panel, now the amplitude scintillation is more significant than in the previous example, producing large values of S4 which coincide with large values of σ_ϕ. This can be seen even though the S4 index has been computed using the SNR

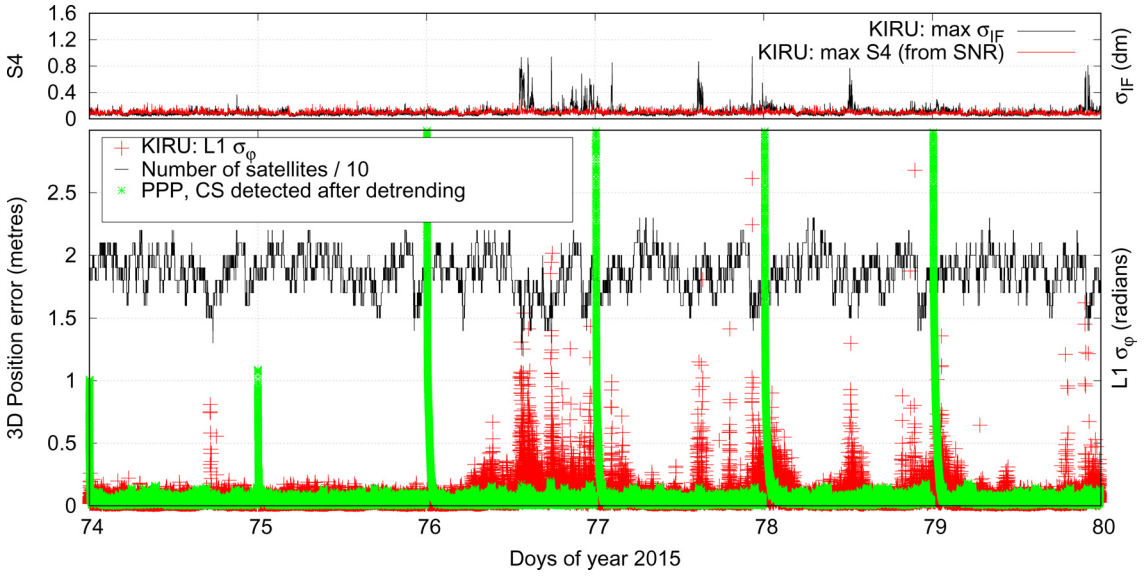

Fig. 7. Navigation solution for the high latitude receiver KIRU during the St. Patrick's day storm (DoYs 76–79, 2015). Top panel: maximum values of S4 and σ_{IF}. Bottom panel: the number of satellites used to compute the navigation solution (divided by 10) is depicted in black. The σ_{ϕ} values are depicted in red and the 3D position error is depicted in green.

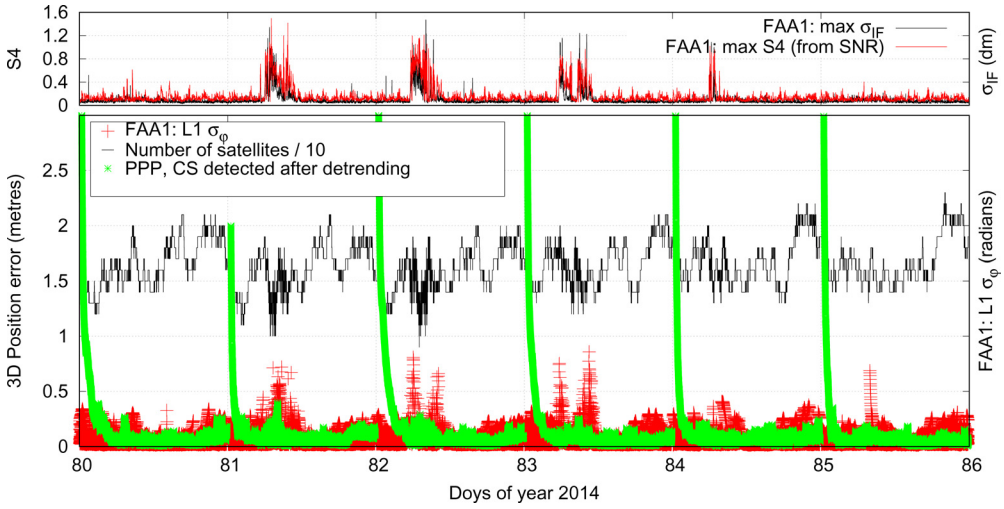

Fig. 8. Navigation solution for the low latitude receiver FAA1 during 6 days on the spring equinox (DoYs 76–79, 2014). Top panel: maximum values of S4 and σ_{IF}. Bottom panel: the number of satellites used to compute the navigation solution (divided by 10) is depicted in black. The σ_{ϕ} values are depicted in red and the 3D position error is depicted in green. Notice that the solution is reset at 0h on each day.

measurement. This result is consistent with previous works (see, for instance, Moraes et al., 2017). Moreover, large values of σ_{IF} are present, also depicted in the top panel. These high S4 and σ_{IF} values confirm the diffractive nature of this type of scintillation. Consequently, unlike the case for the high latitude receiver, one can see in this case that the number of discarded observations increases clearly with the scintillation events. This agrees with the results from Juan et al. (2017) where the carrier phase jumps were associated to the amplitude scintillation, i.e. canonical amplitude fades (Humphreys et al., 2010), which is characteristic in low latitude scintillation. This reduction in the number of satellites with useful observations, i.e. poorer geometry, jointly with the increase of the noise of the L_{IF} combination, as was shown in the previous section, produce an increase of the 3D position error with respect to the error during quiet ionospheric conditions.

Let us explain this situation with a case study. The example corresponds to the receiver FAA1 and the satellite PRN21. The data was collected during the day 081 in 2014. Figure 9 depicts, in red, the residuals of the L_{IF}. As it can be seen, at the beginning of the time interval shown in the plot, there are several cycle slips in L2 (jumps of 37.7 cm) that occur in a nearly continuous way. The presence of these cycle slips impedes to consolidate usable arcs for navigation and, therefore, they must be discarded. This is translated to the

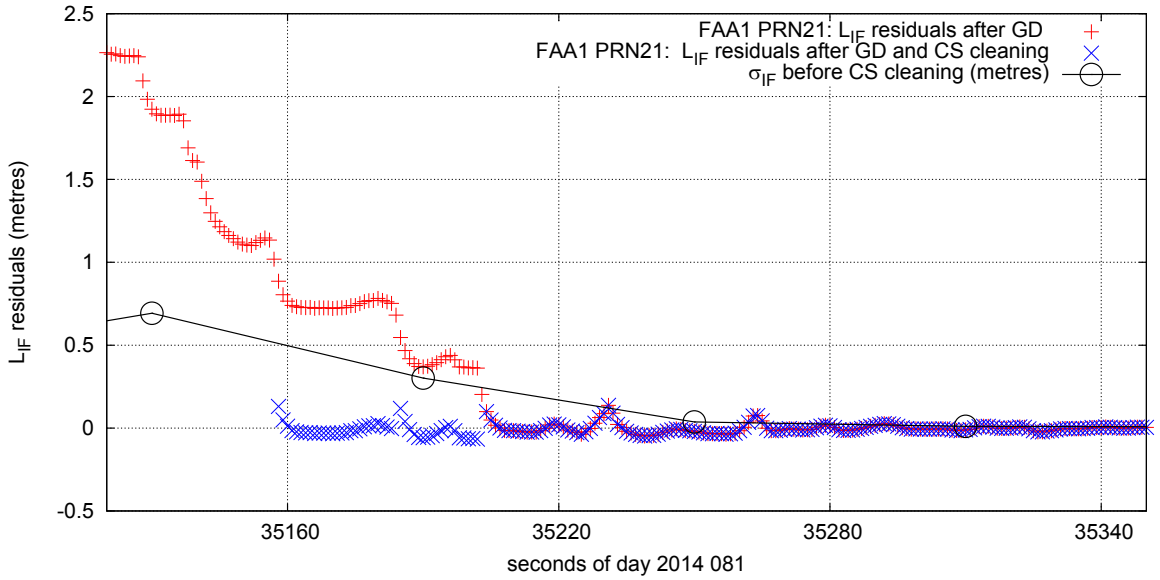

Fig. 9. L_{IF} residuals after applying the geodetic detrending for the receiver FAA1 and the satellite PRN21 during the day 2014 81 (in red). Residuals after discarding non consolidated arcs (in blue). σ_{IF} before detecting cycle slips (in black).

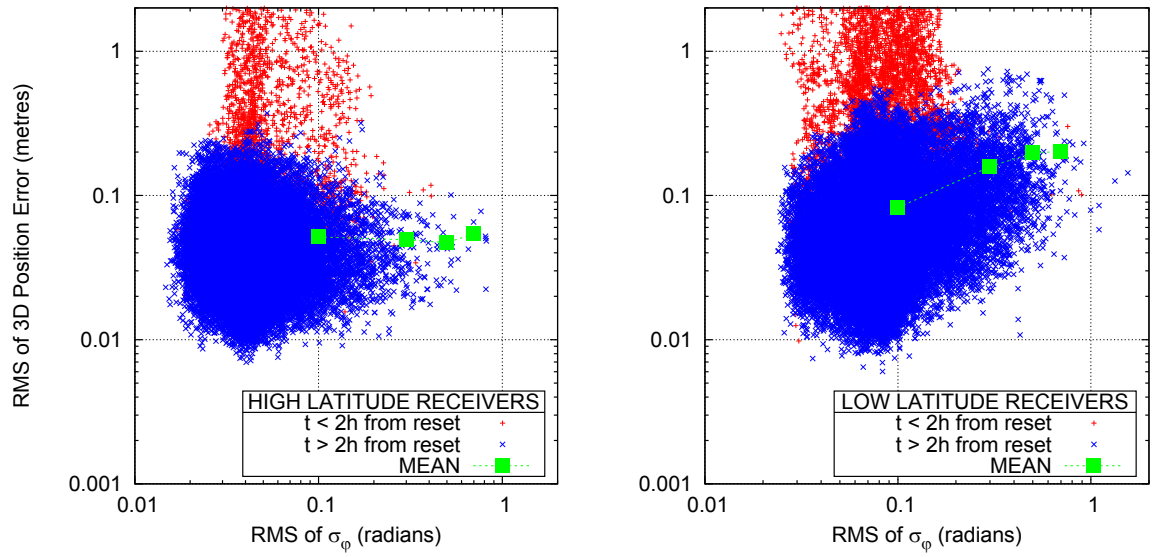

Fig. 10. Relationship between the 3D-position error and the ionospheric scintillation for the 6 IGS receivers shown in Table 1, high latitude receivers are compared in the left panel and low latitude receivers are compared in the right panel. The comparison extends for more than 2 weeks of high ionospheric activity (see Sect. 2). The red points correspond to the first 2 h after the daily reset (convergence period) while the blue points correspond to the comparison during the rest of the day. The green squares depict the mean values of the 3D position error per bins of σ_ϕ (0.1, 0.3, 0.5 and greater than 0.6).

σ_{IF} (in black), which reaches values of several decimetres, being these large values basically due to the uncorrected cycle slips. But this is not the situation for two of these jumps (between the seconds 35150 and 35200) that can be detected and corrected. However, in spite of this detection and correction, the remaining residuals are clearly noisier than the residuals when the measurements are not affected from scintillation (at the end of the time interval). This is the reason why the σ_{IF}, after repairing the cycle slips, still shows large values (close to 10 cm) as it can be seen in the middle panel of Figure 8.

A more general assessment can be done involving all the IGS receivers in Table 1, described in Section 2, is shown in the Figure 10 where the 3D position error is depicted against the ionospheric scintillation activity. In order to compare the results, for each receiver, we have computed the root mean square of the 3D position error (Δr) during 1 min (RMS_{3D}), i.e.:

Table 2. Relationship between $RMS_{\sigma\phi}$ and RMS_{3D} for the receivers included in Table 1. Moreover, the number of cases in the ranges of $RMS_{\sigma\phi}$ are also included.

	KIRU		KIR0		YELL		KOUR		MAL2		FAA1	
$RMS_{\sigma\phi}$ bin	RMS_{3D} (cm)	# of cases	RMS_{3D} (cm)	# of cases	RMS_{3D} (cm)	# of cases	RMS_{3D} (cm)	# of cases	RMS_{3D} (cm)	# of cases	RMS_{3D} (cm)	# of cases
<0.2	4.5	2E4	4.4	2E4	5.6	2E4	7.1	2E4	6.2	2E4	10.8	2E4
0.2–0.4	4.6	111	4.8	60	5.9	44	12.9	243	14.9	1574	19.6	461
0.4–0.6	5.5	11	2.7	3	3.4	6	5.0	6	20.2	293	18.4	46
>0.6	5.7	4	5.1	2	5.0	2	5.0	6	21.3	42		

$$RMS_{3D}^2(t_i) = \frac{1}{60}\sum_{j=0}^{j=59} |\Delta r(t_i + j)|^2$$

and also, for each receiver, we have computed the root mean square of the σ_ϕ ($RMS_{\sigma\phi}$) for all the satellites in view (N_{SATS}) from this receiver, i.e.:

$$RMS_{\sigma_\varphi}^2(t_i) = \frac{1}{N_{SATS}}\sum_{j=1}^{j=N_{SATS}} |\sigma_\varphi^j(t_i)|^2$$

In this way, the figures compare the 1 min RMS of the 3D position error (*Y* axis) with the 1 min RMS of the σ_ϕ (*X* axis). In the figure we have separated, in red, the cases during the first 2 h after the daily reset (which present larger errors due to that the solution has still not converged) from those obtained during the rest of the day that correspond to the converged solution, in blue. Moreover, the JAVAD receivers (KIR0 and YELL) experience some resets in the middle of the day which restart the navigation filter. For that reason, in order to include the comparison results for these two receivers, we have imposed as an additional requirement that the formal error of the navigation solution (that depends only on the geometry) shall be less than 7 cm (for a converged solution this formal error ranges from 4 to 5.5 cm). The comparison for the 3 high latitude receivers are depicted in the left panel and the 3 low latitude ones are compared in the right panel.

As it can be seen in the Figure 10, after the convergence period, the 1 min RMS of the 3D position error is always maintained at the decimetre level. Besides the RMS values, Figure 10 also depicts the mean value of the position error (after the convergence) grouped by bins of the RMS of σ_ϕ: less than 0.2 radians, from 0.2 to 0.4, from 0.4 to 0.6 and greater than 0.6.

From the RMS of the σ_ϕ one can see that, in both cases, the analysed periods include observations under strong scintillation activity. In spite of this, the navigation solution for the high latitude case remains at the same level than during quiet scintillation conditions (5 cm of 3D position error). While for the low latitude case there is a slight increase of the position error with the scintillation activity.

In the low latitude case, there are two reasons for this observed increase on the position error with the σ_ϕ. On one hand, as it is shown in Figure 4, at low latitudes the scintillation effect on the signal does not disappear when the L_{IF} is build, therefore, the position is computed using a noisier measurement. On the other hand, due to the deep amplitude fades associated to low latitude scintillations, cycle slips are much more frequent than in high latitude. Then, in spite of the fact that they can be detected with our technique, there are more measurements which are discarded, as it is shown in Figure 8, and, consequently, the geometry becomes worse affecting the navigation solution.

Table 2 shows the results of Figure 10 separated by receivers. Notice that, both the RMS_{3D} and the $RMS_{\sigma\phi}$, are obtained by averaging values during 1 min or for all the satellites, respectively. Therefore an $RMS_{\sigma\phi}$ greater than (or close to) 1 means that there are several satellites with strong scintillation. For instance, comparing the $RMS_{\sigma\phi}$ values for the FAA1 results in Table 2 with the σ_ϕ values in Figure 8, one can see that there is not any case with $RMS_{\sigma\phi}$ larger than 0.6, but if one observes Figure 8, one can see that there are several events with large phase scintillation (larger than 0.6).

4 Summary

The main conclusions of this work are the following:

We have shown that with the geodetic detrending two of the main effects of scintillation on the GNSS signal can be characterized:

- The presence of cycle slips and also the frequency where these cycle slips occur. As some authors have already shown, if they are not detected, these cycle slips are the responsible of the worsening in the position accuracy under scintillation conditions.
- The increase of noise in the carrier phase. This noise can be measured through the σ_ϕ, obtaining similar values than those obtained from an ISMR. This is a clear advantage taking into account the large number of geodetic receivers working at 1 Hz globally distributed.

In high latitude navigation under scintillation conditions, because amplitude scintillation is not too important, cycle slips are quite rare. Thus, it is possible to navigate with similar accuracies than in quiet ionospheric conditions (around some centimetres). Indeed, we have only found a slight degradation on the navigation solutions related with the scintillation activity.

On the contrary, in low latitude regions amplitude scintillation is also important and the cycle slips, which are associated to the amplitude fades, are more frequent. This fact, in addition to the increase of the noise in the ionospheric free combination, produces a worsening in the navigations accuracy (but just by a factor 2 or 3) during scintillation conditions.

Therefore, the main conclusion of this work is that precise navigation is possible under strong scintillation conditions as long as the problem with the cycle slips could be properly addressed. In this point, it is worth to mention that the geodetic detrending, in our current implementation, works on post-process mode. Hence, it would be interesting to develop algorithms allowing a real time implementation of this methodology.

Acknowledgements. This work was supported in part by the Spanish Ministry of Science and Innovation project CGL2015-66410-P and in part by the European Space Agency project SCIONAV (ESA-ITT 1-8214/15/NL/LvH). Authors acknowledge the use of data from the International GNSS Service. The editor thanks Eurico Rodrigues de Paula and an anonymous referee for their assistance in evaluating this paper.

References

Aarons J. 1982. Global morphology of ionospheric scintillations. *Proc IEEE* **70**: 360–378, DOI:10.1109/PROC.1982.12314.

Aarons J. 1993. The longitudinal morphology of equatorial f-layer irregularities relevant to their occurrence. *Space Sci Rev* **63**: 209–243, DOI:10.1007/BF00750769.

Andalsvik YL, Jacobsen KS. 2014. Observed high-latitude GNSS disturbances during a less-than-minor geomagnetic storm. *Radio Sci* **49**: 1277–1288, DOI:10.1002/2014RS005418.

Béniguel Y, Romano V, Alfonsi L, Aquino M, Bourdillon A, Cannon P, Franceschi, GD, Dubey S, Forte B, Gherm V, Jakowski N, Materassi M, Noack T, Pozoga M, Rogers N, Spalla P, Strangeways H, Warrington EM, Wernik A, Wilken V, Zernov N. 2009. Ionospheric scintillation monitoring and modelling. *Ann Geophys* **52**: 391–416. DOI:10.4401/ag-4595, http://www.annalsofgeophysics.eu/index.php/annals/article/view/4595/4663.

Blewitt G. 1990. An automatic editing algorithm for GPS data. *Geophys Res Lett* **17**: 199–202, DOI:10.1029/GL017i003p00199.

Briggs B, Parkin I. 1963. On the variation of radio star and satellite scintillations with zenith angle. *J Atmos Terr Phys* **25**: 339–366, DOI:10.1016/00219169(63)90150-8, http://www.sciencedirect.com/science/article/pii/0021916963901508.

Cervera MA, Thomas RM. 2006. Latitudinal and temporal variation of equatorial ionospheric irregularities determined from GPS scintillation observations. *Ann Geophys* **24**: 3329–3341, DOI:10.5194/angeo-24-3329-2006, http://www.ann-geophys.net/24/3329/2006/.

Forte B, Radicella SM. 2002. Problems in data treatment for ionospheric scintillation measurements. *Radio Sci* **37**: 1096, DOI:10.1029/2001RS002508, http://onlinelibrary.wiley.com/doi/10.1029/2001RS002508/pdf.

Humphreys T, Psiaki M, Kintner PJ. 2005. GPS carrier tracking loop performance in the presence of ionospheric scintillation. In: Proceedings of ION-GNSS 2005, Long Beach, CA (USA), pp. 156–167, http://www.ion.org/publications/abstract.cfm?articleID=6206.

Humphreys TE, Psiaki ML, Kintner Jr. PM. 2010. Modeling the effects of ionospheric scintillation on GPS carrier phase tracking. *IEEE Trans Aerosp Electron Syst* **46**: 1624–1637, DOI:10.1109/TAES.2010.5595583, http://ieeexplore.ieee.org/document/5595583/.

Jacobsen K, Andalsvik Y. 2016. Overview of the 2015 St. Patrick's day storm and its consequences for RTK and PPP positioning in Norway. *J Space Weather Space Clim* **6**: A9, DOI:10.1051/swsc/2016004.

Jiao Y, Morton YT. 2015. Comparison of the effect of high-latitude and equatorial ionospheric scintillation on GPS signals during the maximum of solar cycle 24. *Radio Sci* **50**: 886–903, DOI:10.1002/2015RS005719, http://onlinelibrary.wiley.com/doi/10.1002/2015RS005719/pdf.

Juan J, Aragon-Angel A, Sanz J, González-Casado G, Rovira-Garcia A. 2017. A method for scintillation characterization using geodetic receivers operating at 1 Hz. *J Geod* **91**: 1383–1397, DOI:10.1007/s00190-017-1031-0.

Moraes AO, Costa E, Abdu MA, Rodrigues FS, de Paula ER, Oliveira K, Perrella WJ. 2017. The variability of low-latitude ionospheric amplitude and phase scintillation detected by a triple-frequency GPS receiver. *Radio Sci* **52**: 439–460, DOI:10.1002/2016RS006165.

Moraes AO, Muella MTAH, de Paula ER, Oliveira CBA, Terra WP, Perrella WJ, Meibach-Rosa PRR. 2017b. Statistical evaluation of GLONASS amplitude scintillation over low latitudes in the Brazilian territory. *Adv Space Res*, ISSN 0273-1177, DOI:10.1016/j.asr.2017.09.032.

Paznukhov VV, Carrano CS, Doherty PH, Groves KM, Caton RG, Valladares CE, Seemala GK, Bridgwood CT, Adeniyi J, Amaeshi LLN, Damtie B, D'Ujanga Mutonyi F, Ndeda JOH, Baki P, Obrou OK, Okere B, Tsidu GM. 2012. Equatorial plasma bubbles and l-band scintillations in Africa during solar minimum. *Ann Geophys* **30**: 675–682, DOI:10.5194/angeo-30-675-2012, http://www.ann-geophys.net/30/675/2012/.

Pi X, Iijima BA, Lu W. 2017. Effects of ionospheric scintillation on GNSS-based positioning. *J Inst Navig* **64**: 3–22, DOI:10.1002/navi.182.

Sanz J, Juan JM, González-Casado G, Prieto-Cerdeira G, Schlueter S, Orús R. 2014. Novel ionospheric activity indicator specifically tailored for GNSS users. In: Proceedings of ION GNSS+. Tampa, Florida (USA), pp. 1173–1182, http://www.ion.org/publications/abstract.cfm?jp=p&articleID=12269.

Skone S, Feng M, Ghafoori F, Tiwari R. 2008. Investigation of scintillation characteristics for high latitude phenomena. In: Proceedings of ION GNSS 2008, Savannah, GA, September 2008, pp. 2425–2433, https://www.ion.org/publications/abstract.cfm?articleID=8144.

Yeh C, Chao-Han L. 1982. Radio wave scintillations in the ionosphere. *Proc IEEE* **70**: 324–360, DOI:10.1109/PROC.1982.12313.

Yunck TP. 1993. Coping with the atmosphere and ionosphere in precise satellite and ground positioning, Environmental Effects on Spacecraft Positioning and Trajectories, vol. 73, pp. 1–16. DOI:10.1029/GM073p0001.

Zumberge JF, Heflin MB, Jefferson DC, Watkins MM, Webb FH. 1997. Precise point positioning for the efficient and robust analysis of GPS data from large networks. *J Geophys Res Solid Earth* **102**: 5005–5017, DOI:10.1029/96JB03860.

Cite this article as: Juan JM, Sanz J, González-Casado G, Rovira-Garcia A, Camps A, Riba J, Barbosa J, Blanch E, Altadill D, Orus R. 2018. Feasibility of precise navigation in high and low latitude regions under scintillation conditions. *J. Space Weather Space Clim.* **8**: A05